

CrystEngComm

Accepted Manuscript



This is an *Accepted Manuscript*, which has been through the Royal Society of Chemistry peer review process and has been accepted for publication.

Accepted Manuscripts are published online shortly after acceptance, before technical editing, formatting and proof reading. Using this free service, authors can make their results available to the community, in citable form, before we publish the edited article. We will replace this *Accepted Manuscript* with the edited and formatted *Advance Article* as soon as it is available.

You can find more information about *Accepted Manuscripts* in the [Information for Authors](#).

Please note that technical editing may introduce minor changes to the text and/or graphics, which may alter content. The journal's standard [Terms & Conditions](#) and the [Ethical guidelines](#) still apply. In no event shall the Royal Society of Chemistry be held responsible for any errors or omissions in this *Accepted Manuscript* or any consequences arising from the use of any information it contains.

Preferential site substitution of Eu^{3+} ions in $\text{Ca}_{10}(\text{PO}_4)_6\text{Cl}_2$ nanoparticles obtained using microwave stimulated wet chemistry technique

Robert Pażik^{1*}, Jean-Marie Nedelec^{2,3} and Rafael J. Wiglusz^{1*}

¹*Institute of Low Temperature and Structure Research, PAS, Okólna 2, 50-422 Wrocław*

²*Clermont Université, ENSCCF, ICCF, BP10448, 63000 Clermont-Ferrand, France.*

³*CNRS, UMR 6296, ICCF, 63171 Aubière, France.*

*Corresponding authors:

R.Wiglusz@int.pan.wroc.pl, R.Pazik@int.pan.wroc.pl;

Phone: +48-71-395-41-59

Fax: +48-71-344-10-29

Homepage address www.int.pan.wroc.pl

Abstract

The Eu^{3+} doped $\text{Ca}_{10}(\text{PO}_4)_6\text{Cl}_2$ nanocrystalline powders were successfully synthesized using microwave stimulated technique. Additional post heat treatment in the temperature range 800 – 1100 °C was applied in order to improve crystallinity of the final product and eliminate residual amorphous phase. Detailed structural characterization was performed by X-ray diffraction (XRD), Raman and infrared (IR) spectroscopy, transmission electron microscopy (TEM) and X-ray fluorescence (EDX). The optical properties of the $\text{Ca}_{10}(\text{PO}_4)_6\text{Cl}_2$ samples doped with different Eu^{3+} concentrations (0.5 – 5 mol%) were determined by measuring excitation, emission spectra and luminescence. TEM images confirmed nanoscale nature of the final product with primary particle size of about 60 nm and hydrodynamic size of 200 nm when product was dispersed in Milli-Q purified water (MQ) without further stabilization. The analysis of the $^5\text{D}_0 \rightarrow ^7\text{F}_0$ transition points out that for low concentration Ca(II) (*A*) site is preferentially substituted whereas increase of Eu^{3+} above 2 mol% results in domination of the Eu^{3+} cations located at Ca(I) (*B*) site. Increase of annealing temperature leads to an increase of the $^5\text{D}_0 \rightarrow ^7\text{F}_0$ intensity associated with the Eu^{3+} at *A* site. Preferential site substitution can be solved by analysis of optical properties of the Eu^{3+} ion. The Judd-Ofelt parameters were calculated using simplified formalisms. The mechanism of concentration quenching process was identified as a dipole-dipole interaction.

Keywords. Nanoparticles, Apatite, Chloroapatite, Structural probe, Preferential substitution.

1. Introduction

Constantly growing interest in development of nanomaterials for advanced bio-applications, such as bio-sensors, involves utilization of highly bio-compatible and photo-stable compounds¹. Materials belonging to the large apatite family described by the general chemical formula $\text{M}_{10}(\text{PO}_4)_6\text{X}_2$ (M – alkaline cations, X – OH^- , Cl^- or F^- anions) are attractive because of their potential application in medicine. Calcium hydroxyapatite $\text{Ca}_{10}(\text{PO}_4)_6(\text{OH})_2$ is the most representative material of the apatite family widely used as biologically safe

material being the main constituent of bones². The use of apatite as bio-marker involves structural modification based on substitution of Ca^{2+} cations with luminescent trivalent rare earth ions (RE^{3+}) delivering excellent photo-stability upon exposure to long-term excitation with UV or NIR irradiation³. The structure of the synthetic apatite compounds is hexagonal, depicted by $P6_3/m$ space group, and offers mainly two cationic sites Ca(I) and Ca(II) for possible substitution with RE^{3+} involving charge compensation mechanism^{4,5}.

Recently our group has conducted a detailed study of the luminescence behaviour of the Eu^{3+} ions in the synthetic $\text{Ca}_{10}(\text{PO}_4)_6(\text{OH})_2$ obtained by wet chemistry technique covering the concentration of optically active ions from 1 to 5mol%^{6,7}. It has been shown that depending on the concentration of dopant and annealing temperature preferential site substitution occurs either at nine-fold coordinated Ca(I) with C_3 symmetry or Ca(II) site with C_s coordinated by seven oxygen anions. In terms of luminescence behaviour Eu^{3+} hydroxyapatite has relatively low quantum efficiency mostly due to the presence of structural OH^- groups causing strong non-radiative energy migration. In this view chloroapatite seems to be more reasonable choice since the absence of OH^- structural units should result in no coupling of the Eu^{3+} ions with OH^- vibrations and therefore enhanced efficiency. It has been already shown that another advantage of chloroapatite application in the bone replacement materials is directly connected with the significant role of chloride ions. The main outcome relies on osteoclasts activation due to the ability of developing local surface acidic environment facilitating the bone resorption process⁸. However strict control of content of the chloroapatite in hydroxyapatite mixture is mandatory to avoid too fast solubilisation of alkaline salts⁹. The calcium chloroapatite $\text{Ca}_{10}(\text{PO}_4)_6\text{Cl}_2$ exists as two polymorphs: at low temperature the apatite crystallizes in a monoclinic phase with space group $P2_1/b$ and after thermal treatment above 350°C ¹⁰ in the typical hexagonal one. Several strategies were developed for the synthesis of apatite particles involving techniques such as microemulsion¹¹, precipitation¹², sol-gel¹³, wet chemistry⁶ and others.

Therefore the aim of the present work was focused on microwave assisted hydrothermal synthesis of nanocrystalline powders of $\text{Ca}_{10}(\text{PO}_4)_6\text{Cl}_2$ doped with Eu^{3+} ions acting both as an optical probe for investigation of structural changes and as luminescent centre adding extra functional properties to the final material which could be further on used as a bio-marker in bone replacement materials.

2. Experimental

The X-ray diffraction (XRD) patterns were measured in a 2θ range of $5 - 100^\circ$ with a X'Pert Pro PANalytical X-ray diffractometer (Cu, $K\alpha_1$: 1.54060 Å). The IR measurements were performed using FT-IR Biorad 575C spectrophotometer. Small amount of chloroapatite powder was dispersed in nujol mull and placed between two highly transparent silicon glasses prior to measurement. Raman measurements were carried out with a Micro-Raman system Renishaw inVia equipped with a confocal Leica DM 2500 M microscope with CCD camera as a detector and a diode laser operating at 830 nm. The spectral resolution was set to 2 cm^{-1} . BET Specific surface area (S_{BET}) was measured by nitrogen gas sorption at 77 K on a Quantachrome Autosorb 1 apparatus. Samples were degassed for 18 h at 100°C before starting. The particle size was calculated from BET measurements using following equation:

$$D = \frac{6}{S_{BET}d}, \quad (1)$$

where D denotes average particle size (μm), S_{BET} is the specific surface area (m^2/g) and d density of investigated material (g/cm^3). Hydrodynamic size was measured using dynamic light scattering technique on Malvern Instruments Zetasizer Nano-ZS instrument operating under He-Ne 633 nm laser and equipped with the Dispersion Technology Software for data collection and analysis. Diluted water dispersions containing chloroapatite were each time equilibrated for 2 minutes before starting the actual measurement. The values of refractive index and absorbance were taken, for the $\text{Ca}_{10}(\text{PO}_4)_6\text{Cl}_2$, from literature. Additionally hydrodynamic size was measured by using Nanosight NS 500 automated instrument using 405 nm line of laser diode as a light source backscattered further on measured objects. The samples for hydrodynamic size measurements were prepared by taking 1 ml of water suspension containing nanoparticles and further on diluted with 19 ml of de-ionized water and transferred by peristaltic pumps to the sample chamber. Typically the starting concentration of nanoparticles in all prepared suspensions was around $500\ \mu\text{g}/\text{ml}$. Each measurement was repeated at least three times and conducted with different dilution of particles to achieve satisfactory statistics and exclude errors connected with too high or too low amount of analyzed objects. From simultaneous measurement of the mean squared displacement of each particle tracked, the particle diffusion coefficient (D_t) and hence sphere-equivalent, hydrodynamic radius (r_h) can be determined using the Stokes-Einstein equation:

$$r_h = \frac{K_B T}{6\pi\eta D_t}, \quad (2)$$

where K_B is Boltzmann's constant, T is temperature and η is solvent viscosity (H_2O). The analysis was done using Nanosight NTA 2.3 software allowing for determination of the

particle/object concentration represented as a number of the particles/objects per mL. The $\text{Ca}_{10}(\text{PO}_4)_6\text{Cl}_2:\text{Eu}^{3+}$ powders were investigated by the transmission electron microscopy (TEM) using Philips CM-20 SuperTwin microscope, operating at 200 kV. Specimens for HRTEM were prepared by dispersing small amount of sample in methanol and putting a droplet of the suspension on a copper microscope grid covered with perforated carbon. The elemental analyses were carried out using a scanning electron microscope FEI Nova NanoSEM 230 equipped with EDS spectrometer (EDAX PegasusXM4). Up to 10 measurements were made from different random areas for each sample to assure satisfactory statistics. The luminescence spectra were recorded using Jobin Yvon THR1000 monochromator equipped with Hamamatsu R928 photomultiplier and 1200 lines/mm grating blazed at 500 nm. As an excitation source continuous 266 nm line of YAG:Nd laser (third harmonics) was used. Excitation spectra were measured using Spectra Pro 750 monochromator, equipped with Hamamatsu R928 photomultiplier and 1200 l/mm grating blazed at 500 nm. The 450 W xenon arc lamp was used as an excitation source. It was coupled with 275 mm excitation monochromator, which used a 1800 l/mm grating blazed at 250 nm. The lifetimes were measured utilizing LeCroy oscilloscope after 266 nm excitation with pulse YAG:Nd laser. All recorded spectra were corrected accordingly to the apparatus characteristic.

Synthesis of $\text{Ca}_{10}(\text{PO}_4)_6\text{Cl}_2:\text{Eu}^{3+}$ nanoparticles. The main substrates used for the fabrication of the $\text{Ca}_{10}(\text{PO}_4)_6\text{Cl}_2$ nanoparticles doped with different concentrations of Eu^{3+} ions (0.5 – 5 mol%) using microwave stimulated hydrothermal technique were CaCl_2 (99.9 % Alfa Aesar), $(\text{NH}_4)_2\text{HPO}_4$ (99.99% Sigma Aldrich), Eu_2O_3 (99.99% Alfa Aesar) as well as NH_4OH (99 % Avantor Poland) for pH control. In a typical preparation procedure *i.e.* for the final product containing 1 mol% of the Eu^{3+} , the stoichiometric amount of the Eu_2O_3 0.01583 g (0.045 mmol) was first digested in an excess of the HNO_3 (ultrapure Avantor Poland) in order to transform europium oxide into the water soluble europium nitrate. The $\text{Eu}(\text{NO}_3)_3 \cdot 6\text{H}_2\text{O}$ was further on re-crystallized three times to get rid of the HNO_3 excess. Afterwards 0.9889 g (8.91 mmol) of CaCl_2 was dissolved in MQ-water together with $\text{Eu}(\text{NO}_3)_3$. Subsequently 0.8319 g (6.3 mmol) of $(\text{NH}_4)_2\text{HPO}_4$ was added to the mixture resulting in fast precipitation of the by-product. The pH of the dispersion was adjusted to 11 with NH_4OH , transferred into the Teflon vessel and placed in the microwave reactor (ERTEC MV 02-02). After 90 min of the microwave stimulated hydrothermal processing at 200°C and under autogenous pressure of 50 atm. Resulting white powder was washed with de-ionized

water and dried at 60°C for 24 h. In order to force full crystallization and get rid of amorphous phase a final thermal treatment was then applied in the temperature range of 800 – 1100°C.

3. Results and Discussion

Structure analysis.

The evolution of the $\text{Ca}_{10}(\text{PO}_4)_6\text{Cl}_2:\text{Eu}^{3+}$ crystalline phase was followed by XRD both as a function of annealing temperature (see Figure 1) and concentration of the optically active ions (see Figure 2). As it can be seen pure hexagonal phase of $\text{Ca}_{10}(\text{PO}_4)_6\text{Cl}_2$ is present at 800°C¹⁴. Below this temperature sample is a mixture of the chloroapatite, an amorphous phase and contains small amount of the europium(III) phosphate (EuPO_4). The incorporation/diffusion of the Eu^{3+} into the $\text{Ca}_{10}(\text{PO}_4)_6\text{Cl}_2$ crystal structure can be achieved only by delivering more energy into the system *i.e.* higher temperature of treatment. Increase of the annealing temperature up to 1100°C results in enhancement of the powder crystallinity and particle growth. No phase decomposition was observed within the explored temperature range. In the case of the dopant effect one can observe that up to 2 mol% of the Eu^{3+} no additional phase is present whereas sample containing 5 mol% of the Eu^{3+} shows traces of the EuPO_4 phase visible at around 29°¹⁵. The appearance of the extra phase at higher levels of dopant concentration might point out the critical solubility of the Eu^{3+} in the $\text{Ca}_{10}(\text{PO}_4)_6\text{Cl}_2$ phase due to the difference in ionic radii (Ca^{2+} (CN₉) - 1.18 Å, Eu^{3+} (CN₉) - 1.12 Å, Ca^{2+} (CN₇) - 1.06 Å, Eu^{3+} (CN₇) - 1.01 Å) and valence incompatibility between Ca^{2+} and Eu^{3+} cations¹⁶. This is also consistent with observation done by Fleet⁹ *et.al.* claiming that solubility of the RE^{3+} ions is up to two orders of magnitude lower in the $\text{Ca}_{10}(\text{PO}_4)_6\text{Cl}_2$ than $\text{Ca}_{10}(\text{PO}_4)_6(\text{OH})_2$. In fact, in our previous studies the solubility of Eu^{3+} ions in the hydroxyapatite phase was found to be higher⁶. The thorough structural analysis (see Figure 3) was performed based upon Rietveld method¹⁷ using isotropic approach^{18,19} in Maud 2.0 software²⁰. Final results were compared with the literature data and gathered in Tables 1 and 2. There is no straightforward dependence of the individual cell parameters or cell volume (a , c and V) on temperature nor dopant concentration within set ranges. On the one hand the average size of crystallites is influenced by sintering temperature, as a result of well known Ostwald ripening process, being around 80 nm for the $\text{Ca}_{10}(\text{PO}_4)_6\text{Cl}_2$ treated at 800°C and more than 180 nm above 1000°C. On the other hand no concentration effect connected with Eu^{3+} cations substitution on the growth of the particles was found resulting in average size close to 80 nm whatever the doping level. Based on the XRD analysis the samples heat treated at 800°C were selected for further studies as their particle size lies within range of

nanotechnology interest. The particle size estimation using BET surface area measurement gave comparable results with the Rietveld calculations leading to the value of 110 nm ($S_{BET} = 16 \text{ m}^2/\text{g}$, $d_{CaPO_4} = 3.20 \text{ g}/\text{cm}^3$).

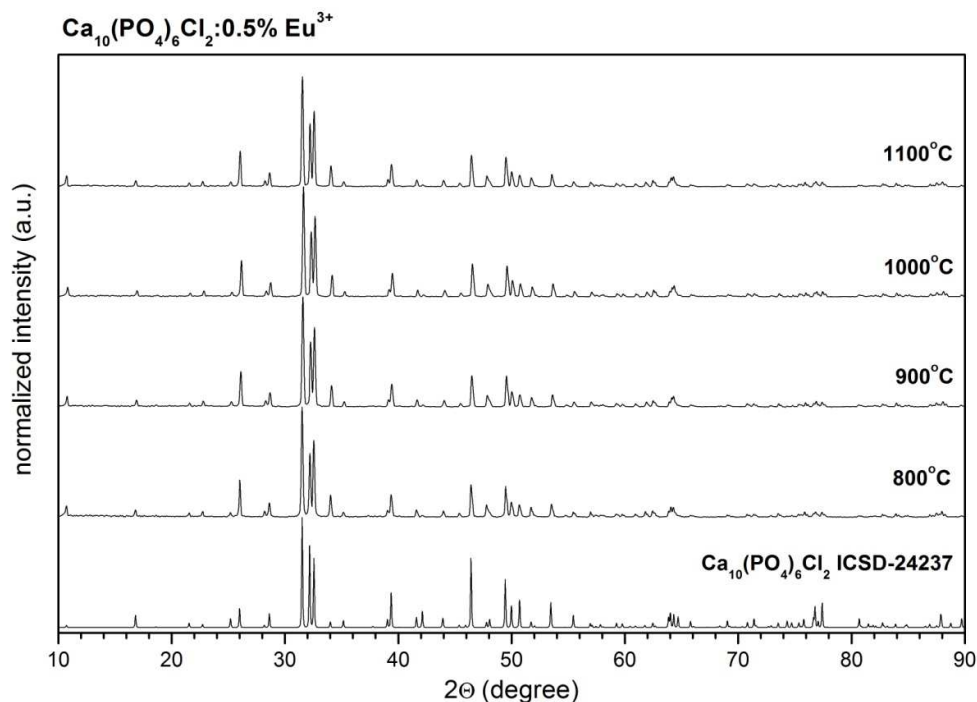


Figure 1. XRD patterns of the $\text{Ca}_{10}(\text{PO}_4)_6\text{Cl}_2:0.5\% \text{Eu}^{3+}$ samples annealed at various temperatures.

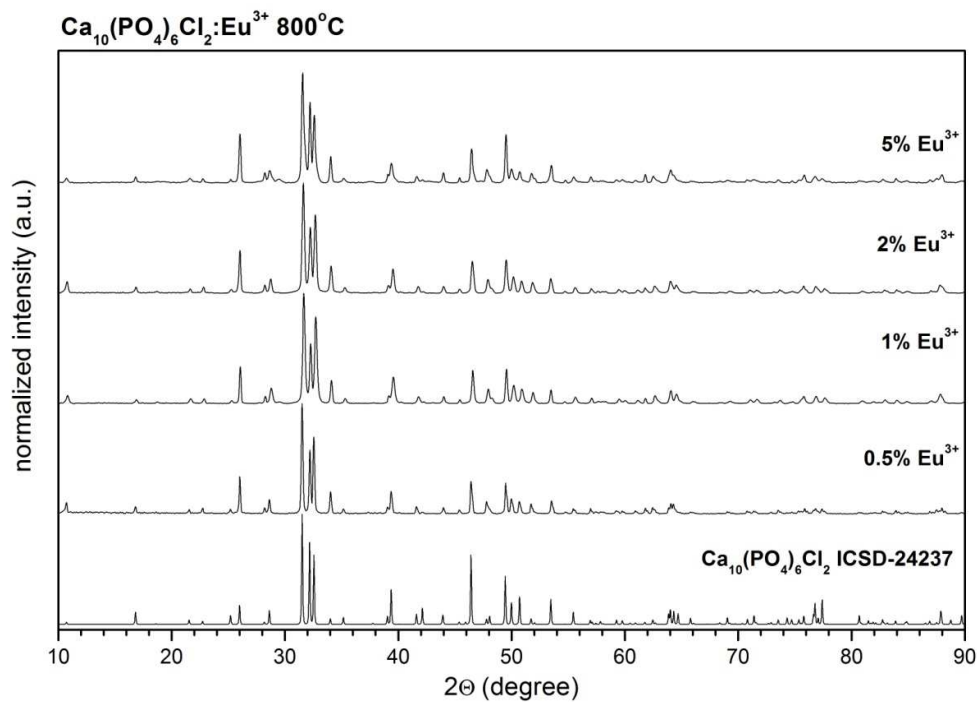
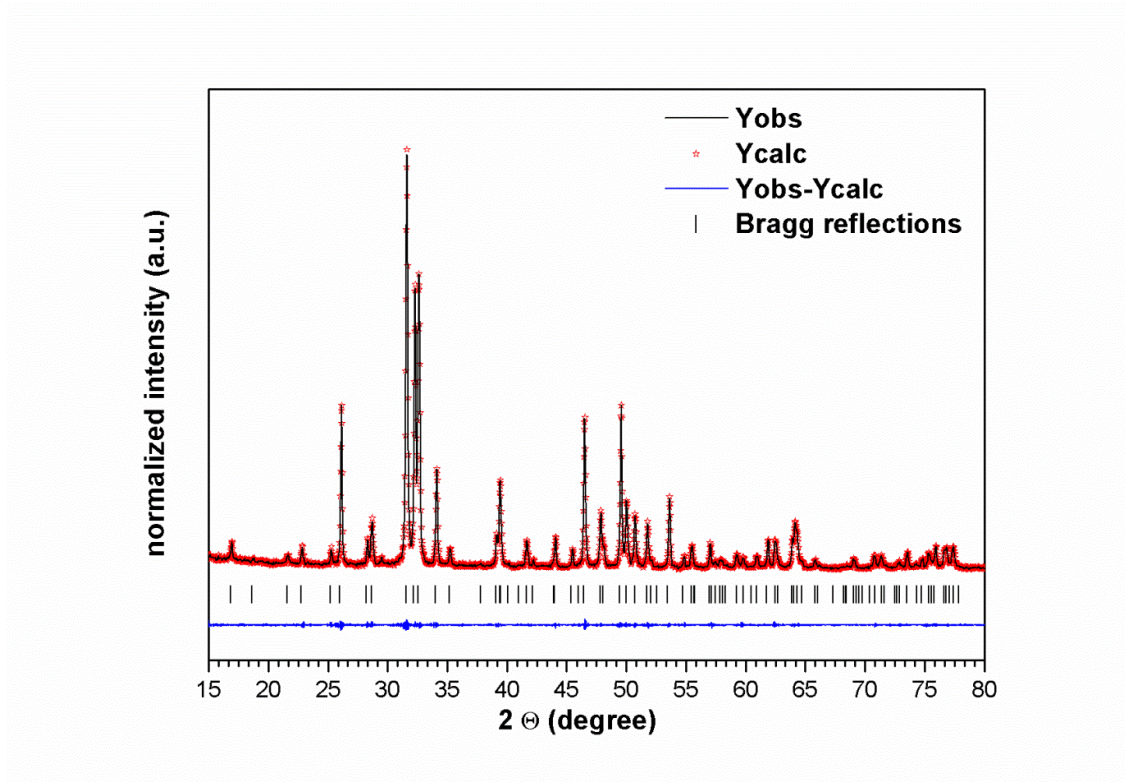


Figure 2. XRD patterns of the $\text{Ca}_{10}(\text{PO}_4)_6\text{Cl}_2:\text{Eu}^{3+}$ samples for various dopant concentration treated at 800°C .Figure 3. Representative results of the of the $\text{Ca}_{10}(\text{PO}_4)_6\text{Cl}_2:1\% \text{Eu}^{3+}$ Rietveld analysis (red – fitted diffraction; blue – differential pattern, column – reference phase peak position).Table 1. Unit cell parameters (a,c), cell volume (V), grain size as well as refine factor (R_w) for the $\text{Ca}_{10}(\text{PO}_4)_6\text{Cl}_2:0.5\% \text{Eu}^{3+}$ powder as function of temperature treatment.

| Sample | a (Å) | c (Å) | V (Å ³) | size (nm) | R_w (%) |
|----------------|---------|---------|---------------------|-----------|-----------|
| single crystal | 9.52(3) | 6.85(3) | 537.64(3) | – | – |
| 800°C | 9.54(6) | 6.85(4) | 539.90(6) | 81 | 4.5 |
| 900°C | 9.61(1) | 6.80(3) | 543.85(9) | 101 | 4.7 |
| 1000°C | 9.59(6) | 6.81(1) | 542.39(4) | 172 | 4.2 |
| 1100°C | 9.55(9) | 6.82(6) | 538.66(9) | 190 | 4.6 |

Table 2. Unit cell parameters (a,c), cell volume (V), grain size as well as refine factor (R_w) for the $\text{Ca}_{10}(\text{PO}_4)_6\text{Cl}_2:\text{Eu}^{3+}$ nanoparticles treated at 800°C .

| Sample | a (Å) | c (Å) | V (Å ³) | size (nm) | R _w (%) |
|-----------------------|---------|---------|---------------------|-----------|--------------------|
| 0.5% Eu ³⁺ | 9.54(6) | 6.85(4) | 539.90(6) | 81 | 4.5 |
| 1% Eu ³⁺ | 9.51(0) | 6.86(7) | 537.29(9) | 90 | 5.9 |
| 2% Eu ³⁺ | 9.57(1) | 6.83(7) | 541.72(0) | 70 | 4.3 |
| 5% Eu ³⁺ | 9.52(1) | 6.85(5) | 537.64(4) | 86 | 4.5 |

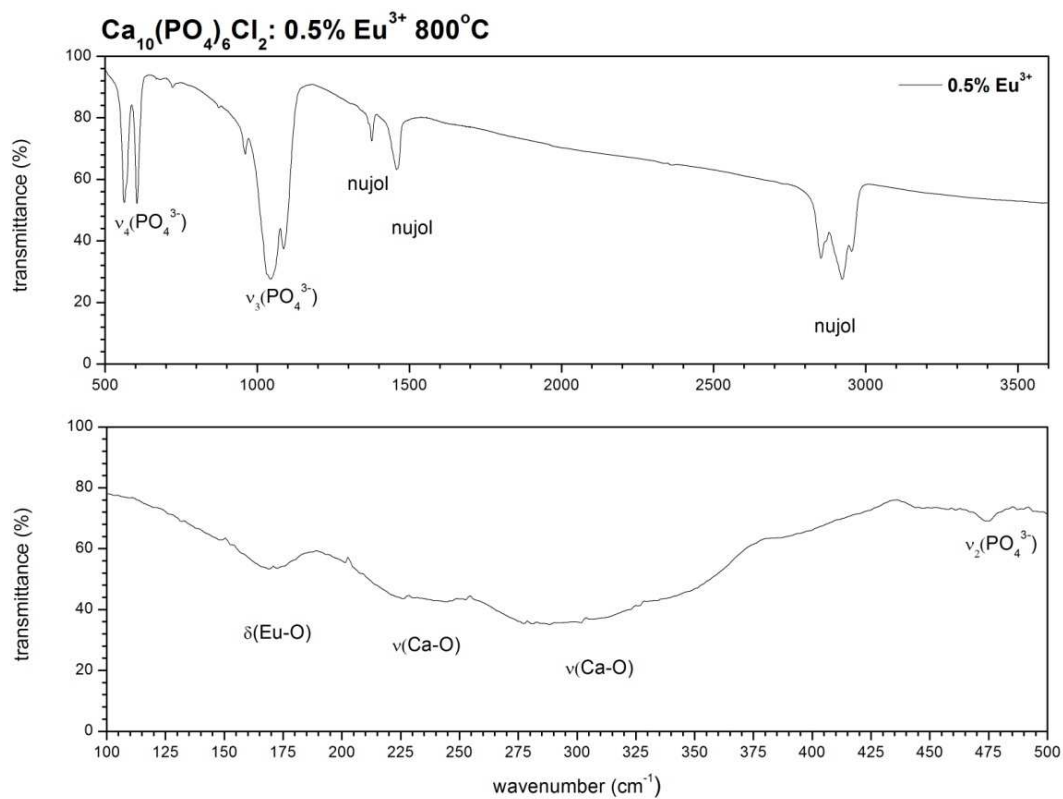


Figure 4. Representative IR spectrum of the Ca₁₀(PO₄)₆Cl₂: 0.5% Eu³⁺ heat treated at 800°C.

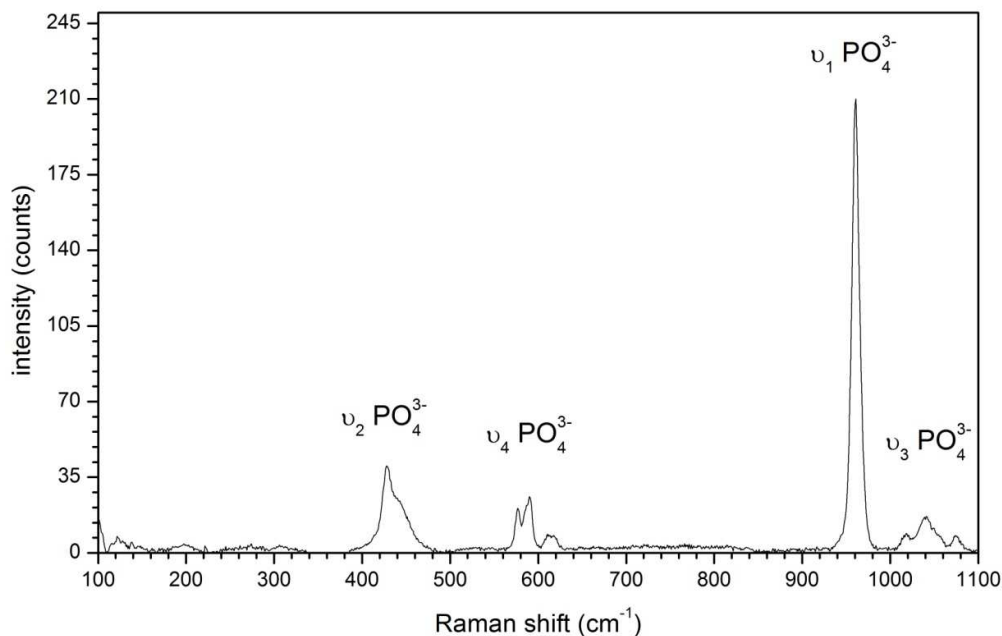


Figure 5. Representative Raman spectrum of the $\text{Ca}_{10}(\text{PO}_4)_6\text{Cl}_2:1\% \text{Eu}^{3+}$ heat treated at 800°C .

The infrared absorption (IR) and Raman spectra (see Figures 4 and 5) were recorded in order to get a more detailed insight into structural peculiarities of the $\text{Ca}_{10}(\text{PO}_4)_6\text{Cl}_2:\text{Eu}^{3+}$ compound. Actually the IR spectra consists of a typical active vibrational bands related to the phosphate PO_4^{3-} species at 469 cm^{-1} , 564 cm^{-1} , 607 cm^{-1} , 962 cm^{-1} , 1043 cm^{-1} , 1087 cm^{-1} as well as vibrations of the Eu-O at 173 cm^{-1} and Ca-O at 230 cm^{-1} and 308 cm^{-1} clearly indicating the presence of pure apatite structure²¹. Additionally, a lack of the characteristic vibrations at 3560 cm^{-1} and 630 cm^{-1} due to the hydroxyl stretch and libration of OH^- groups was found confirming formation of the pure chloroapatite structure²². The additional peaks located at around 1377 cm^{-1} , 1461 cm^{-1} , 2848 cm^{-1} , 2919 cm^{-1} and 2954 cm^{-1} are due to the nujol mull. In the case of Raman spectra four typical vibrational modes of the PO_4^{3-} unit are observed easily at 961 cm^{-1} attributed to the ν_1 mode, three overlapping bands at 1019 cm^{-1} , 1040 cm^{-1} and 1076 cm^{-1} associated with the ν_3 , group of peaks at 575 cm^{-1} , 588 cm^{-1} and 615 cm^{-1} ascribed to the ν_4 as well as asymmetric band with maximum at 426 cm^{-1} due to the ν_2 mode, respectively. All of the mode position are essentially the same as reported by Feki *et.al.*²¹ confirming structural purity of the final product.

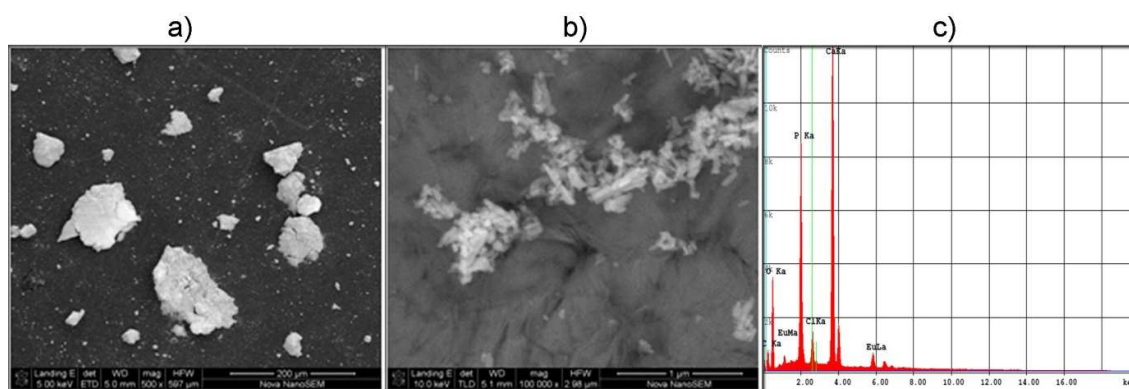


Figure 6. SEM-EDS characterization of the of the $\text{Ca}_{10}(\text{PO}_4)_6\text{Cl}_2:0.5\% \text{Eu}^{3+}$ heat treated at 800°C .

EDS analysis (see Figure 6c) provides direct evidence of the presence of Cl^- anions in the studied samples confirming their expected elemental compositions. The resulting contents of the respective elements were in good correspondence with theoretical values with small 2-5 % deviation arising from the typical error sources of the EDS technique²³. In the case of the Eu^{3+} cations the end value for the low concentrated samples is associated with higher error and is not reliable due to the detection limits.

Morphology and particle sizing techniques.

The size of the $\text{Ca}_{10}(\text{PO}_4)_6\text{Cl}_2:\text{Eu}^{3+}$ particles was analyzed using two different approaches in order to compare them and to aim better the final product for applications. On one hand so-called primary size of particles, broadly discussed previously^{24,25}, was estimated on dry powders using TEM microscopy (Figure 7). On the other hand water based colloidal suspensions containing re-dispersed $\text{Ca}_{10}(\text{PO}_4)_6\text{Cl}_2:\text{Eu}^{3+}$ particles were characterized by the DLS technique (see Figure 8). The former approach would give information regarding overall outlook on the form of the final powder, its shape and primary size whereas the latter one could give straight answer regarding the usefulness of the desired material for the bio-related applications delivering particle hydrodynamic size. Hence, in accordance with TEM analysis (see Figures 7a and 7b) the $\text{Ca}_{10}(\text{PO}_4)_6\text{Cl}_2:\text{Eu}^{3+}$ powder sample contains loosely agglomerated particles with regular and often elongated shapes. The primary size is 60 nm with rather broad distribution characteristic of all materials where high temperature thermal treatment is involved²⁶. Analysis of the SAED image (see Figure 7c) points out on the presence of well developed spotty rings confirming high level of material crystallization at positions expected for the pure hexagonal $\text{Ca}_{10}(\text{PO}_4)_6\text{Cl}_2$ phase.

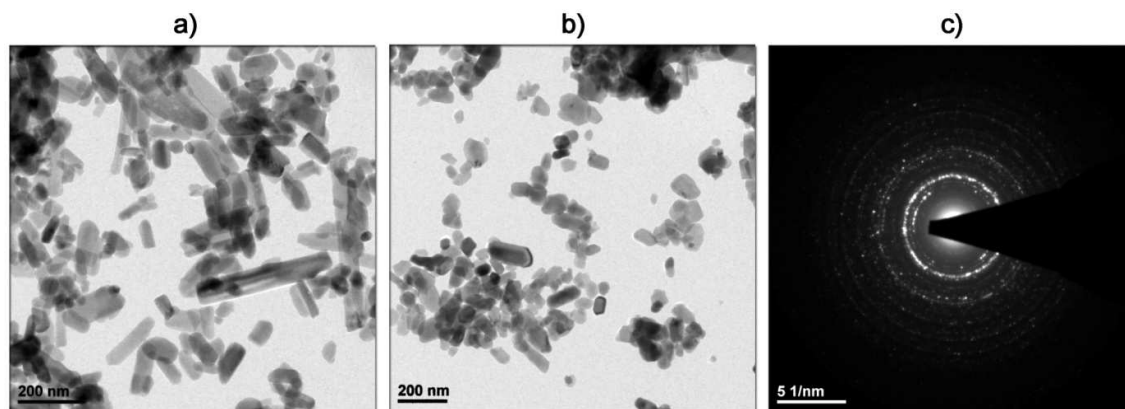


Figure 7. TEM images of the (a) $\text{Ca}_{10}(\text{PO}_4)_6\text{Cl}_2: 0.5\% \text{Eu}^{3+}$, (b) $\text{Ca}_{10}(\text{PO}_4)_6\text{Cl}_2: 5\% \text{Eu}^{3+}$ and SAED picture of the $\text{Ca}_{10}(\text{PO}_4)_6\text{Cl}_2: 0.5\% \text{Eu}^{3+}$ sintered at 800°C .

As it has been mentioned earlier in order to recognize the state of the particle in water suspensions it is necessary to follow the hydrodynamic size which could be critical for certain bio-related applications. Therefore colloids containing $\text{Ca}_{10}(\text{PO}_4)_6\text{Cl}_2$ nanoparticles with 2 mol% of Eu^{3+} ions were prepared and measured using two different instruments Malvern Zetasizer and Nanosight NS 500. As it can be seen in Figure 8 obviously the $\text{Ca}_{10}(\text{PO}_4)_6\text{Cl}_2$ nanoparticles are present in the dispersion as agglomerates containing at least four particles with the average size of 200 nm. The inset in Figure 8 presents results of measurement on Zetasizer instrument (upper inset) as well. Both results are actually comparable. However, the result of measurement on Malvern instrument points out on existence of higher particles fraction with size below 100 nm whereas size distribution remains the same. The bottom inset in Figure 8 shows a first frame of the 30 sec video made for image analysis using NTA software.

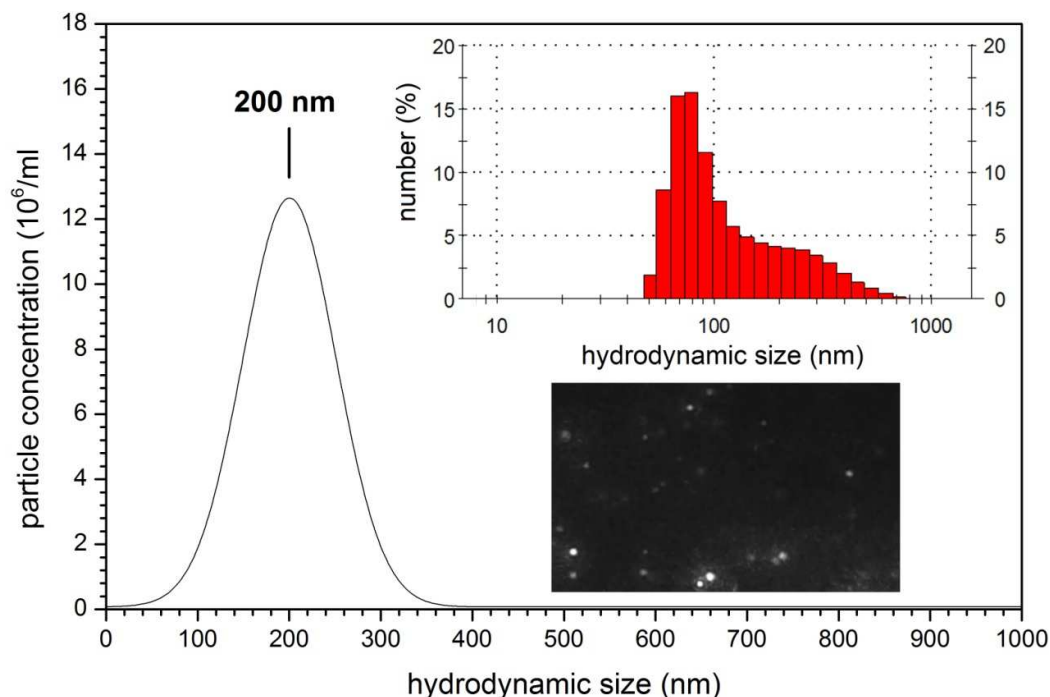


Figure 8. Comparison of the particle size and distribution of the $\text{Ca}_{10}(\text{PO}_4)_6\text{Cl}_2: 0.5\% \text{Eu}^{3+}$ DLS techniques with Nanosight NS 500 and Malvern Zetasizer (inset). Right-bottom image shows the first frame of 60 sec video recorder for image analysis.

Optical properties

The $\text{Ca}_{10}(\text{PO}_4)_6\text{Cl}_2:\text{Eu}^{3+}$ excitation spectra, were measured at 300 K monitoring emission wavelength at 617 nm as a function of dopant concentration corresponding accurately with the maximum intensity of the $^5\text{D}_0 \rightarrow ^7\text{F}_2$ electric dipole transition (see Figure 9). In general, excitation emission spectra consist of typical absorption bands of the Eu^{3+} ion with the broad band emission in the UV spectral region ascribed to the $\text{O}^{2-} \rightarrow \text{Eu}^{3+}$ charge transfer band (CT) as well as sharp intra-configurational $f-f$ lines. Therefore, narrow band located at $27\,694 \text{ cm}^{-1}$ (361 nm) was attributed to the $^7\text{F}_0 \rightarrow ^5\text{L}_{10,9,8}, ^5\text{D}_4$ transitions, at $26\,672 \text{ cm}^{-1}$ (375 nm) $^7\text{F}_0 \rightarrow ^5\text{G}_{2,3}, ^5\text{L}_7$, at $25\,437 \text{ cm}^{-1}$ (394 nm) $^7\text{F}_0 \rightarrow ^5\text{L}_6$ and at $21\,606 \text{ cm}^{-1}$ (462 nm) $^7\text{F}_0 \rightarrow ^5\text{D}_2$, respectively. Since the f orbitals of lanthanide ions are well isolated the electron transitions occurring within f shell are weakly influenced by the ligand field. In consequence position of the peaks remain almost constant regardless on the compound type. As it could be seen in the Figure 9 the positions of the $f-f$ transitions do not change at all with increase of the Eu^{3+} concentration (please see dashed black line). However, a quite different situation occurs when analyzing the CT band location. Taking into account crystallographic data of the $\text{Ca}_{10}(\text{PO}_4)_6\text{Cl}_2$ doped with Eu^{3+} ion can theoretically be incorporated at both Ca^{2+} sites.

Firstly, 9-fold coordinated Ca(II), depicted for clarity as *A* crystallographic position, secondly 7-fold coordinated Ca(I), *B* site in this paper, where seven O^{2-} anions form a coordination polyhedron. As it can be seen for the most diluted sample (0.5 mol% Eu^{3+} ions) the barycenter of the CT band is located at $43\,488\text{ cm}^{-1}$ (230 nm) whereas increase of the Eu^{3+} ions concentration up to 5 mol% shifts CT band towards lower energies $42\,322\text{ cm}^{-1}$ (236 nm). Another characteristic feature is that the CT band observed in all spectra is asymmetric. According to the literature the energy of the the $O^{2-} \rightarrow Eu^{3+}$ CT is driven by the stabilization of O^{2-} ions by surrounding cations. The smaller the cation radius and the higher the charge as well as higher coordination number, the larger the stabilization is and thus blue-shifted CT energy²⁷. Therefore, lower nephelauxetic effect is anticipated for the *A* site with 9 fold coordination in comparison with *B* site with 7 fold coordination. Eventually position of the CT band for the less concentrated $Ca_{10}(PO_4)_6Cl_2 \cdot 0.5\% Eu^{3+}$ would be definitely located at higher energies since preferential substitution occurs at *A* crystallographic site. The red shift and asymmetric shape of the CT band upon increase of the Eu^{3+} ions concentration would be caused by incorporation of the Eu^{3+} ions at *B* site. The Eu^{3+} cations excitation behavior is strongly supported by the analysis of the emission spectra delivering further evidence to discussed issues.

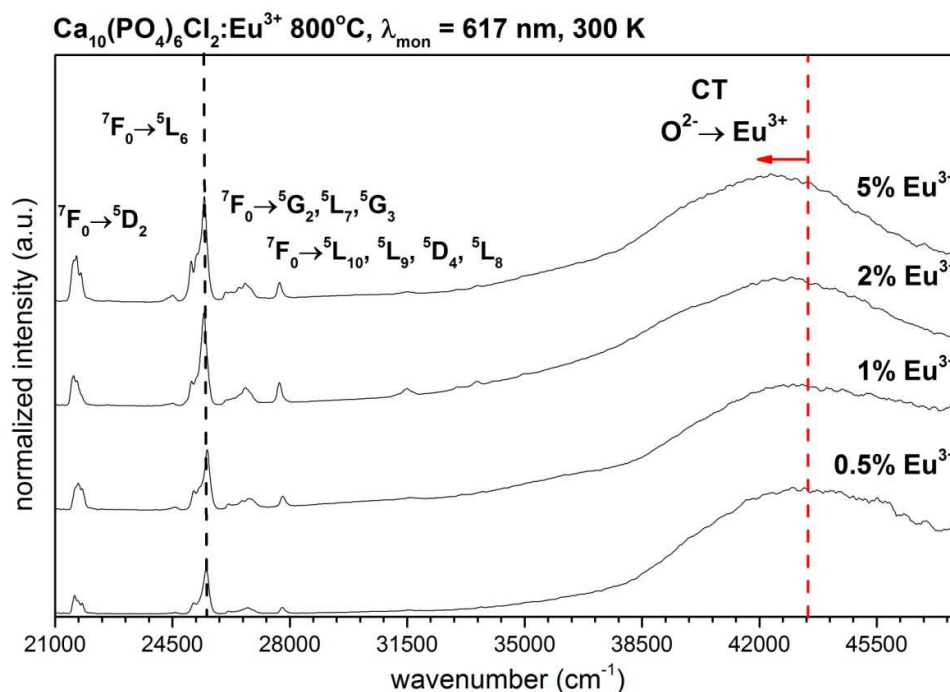


Figure 9. Excitation emission spectrum of the $Ca_{10}(PO_4)_6Cl_2 \cdot Eu^{3+}$ as function of dopant concentration measured at 300 K , $\lambda_{mon} = 617\text{ nm}$.

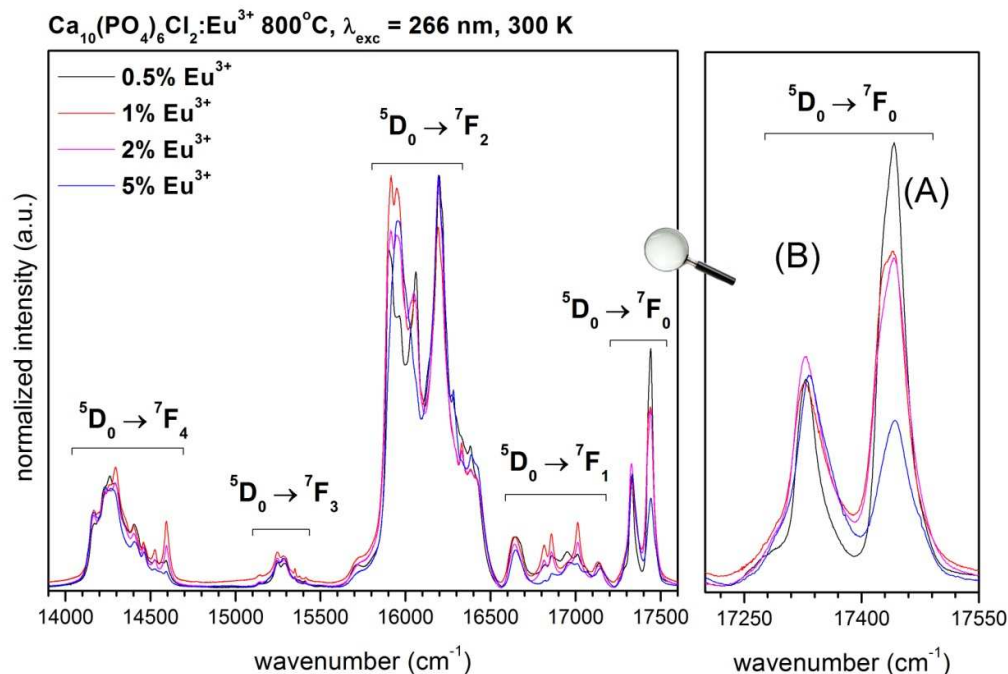


Figure 10. Emission spectrum of the $\text{Ca}_{10}(\text{PO}_4)_6\text{Cl}_2:\text{Eu}^{3+}$ samples as a function of dopant concentration measured at 300 K, $\lambda_{\text{exc}} = 266$ nm.

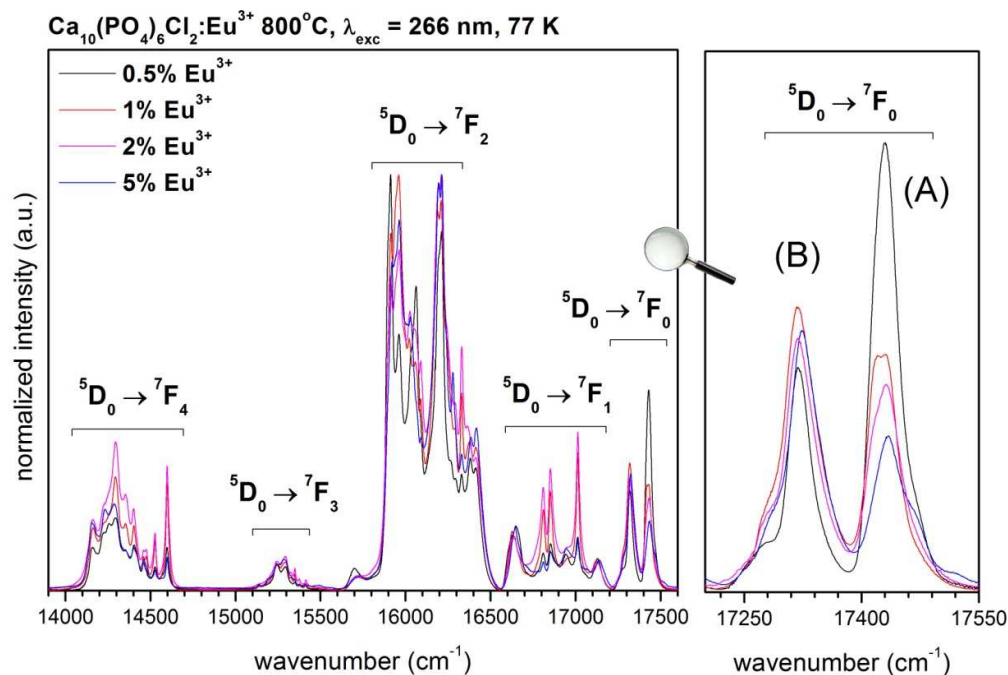


Figure 11. Emission spectrum of the $\text{Ca}_{10}(\text{PO}_4)_6\text{Cl}_2:\text{Eu}^{3+}$ samples as a function of dopant concentration measured at 77 K, $\lambda_{\text{exc}} = 266$ nm.

Figures 10 and 11 present the emission spectra of the $\text{Ca}_{10}(\text{PO}_4)_6\text{Cl}_2:\text{Eu}^{3+}$ samples collected at 300 K and 77 K upon excitation at 266 nm as a function of the Eu^{3+} ions

concentration (1-5%mol) corrected accordingly to the apparatus response. The discussion of the Eu^{3+} ions luminescent behavior already found a special place in the scientific literature since it can be indicative of structural disorders^{28,29}, phase transitions³⁰ and of course finds application as a phosphor material³¹. Typically emission spectra of the Eu^{3+} consists of characteristic bands in the visible region ascribed to the specific electron transitions occurring within the $f-f$ shell of Eu^{3+} ions. In most cases, the ${}^5\text{D}_0 \rightarrow {}^7\text{F}_{0-4}$ transitions are observed as a result of the depopulation of the lowest lying meta-stable excited ${}^5\text{D}_0$ level to the respective crystal field components of the ${}^7\text{F}_{0-4}$ levels of the ${}^7\text{F}$ ground term. The electron transition like ${}^5\text{D}_0 \rightarrow {}^7\text{F}_{5,6}$ usually have low intensity and are difficult to detect. Nevertheless, the emission from the ${}^5\text{D}_1$ or ${}^5\text{D}_2$ excited states could be also recorded especially in the case of low phonon crystal matrices *i.e.* fluorides³². In the case of the $\text{Ca}_{10}(\text{PO}_4)_6\text{Cl}_2:\text{Eu}^{3+}$ emission spectra one can observe two evidently separated lines with maximum at $17\,442\text{ cm}^{-1}$ (573.3 nm), $17\,329\text{ cm}^{-1}$ (577 nm) both corresponding to the ${}^5\text{D}_0 \rightarrow {}^7\text{F}_0$ transitions, at $17\,011\text{ cm}^{-1}$ (587.8 nm) to the ${}^5\text{D}_0 \rightarrow {}^7\text{F}_1$, at $16\,195\text{ cm}^{-1}$ (617.4 nm) to the ${}^5\text{D}_0 \rightarrow {}^7\text{F}_2$, at $15\,249\text{ cm}^{-1}$ (655.7 nm) to the ${}^5\text{D}_0 \rightarrow {}^7\text{F}_3$ as well as at $14\,297\text{ cm}^{-1}$ (699.7 nm) to the ${}^5\text{D}_0 \rightarrow {}^7\text{F}_4$ transition, respectively. From the nature of the ${}^7\text{F}_0$ ground state and the excited ${}^5\text{D}_0$ level being non-degenerated under any symmetry, analysis of this transition gives information regarding number of crystallographically independent Eu^{3+} ions existing in the given host lattice. Taking into account structural data and possibility of incorporation of the Eu^{3+} ions into both Ca^{2+} cations sites *A* and *B* presence of the two ${}^5\text{D}_0 \rightarrow {}^7\text{F}_0$ transitions strongly supports this fact and it is consistent with excitation spectra observation. In accordance with the rule of $2J + 1$ at C_s symmetry a maximum of five sublevels should be present for the ${}^5\text{D}_0 \rightarrow {}^7\text{F}_1$ and eight in the case of the ${}^5\text{D}_0 \rightarrow {}^7\text{F}_2$ transitions whereas at C_3 symmetry the ${}^5\text{D}_0 \rightarrow {}^7\text{F}_1$ splits into two and the ${}^5\text{D}_0 \rightarrow {}^7\text{F}_2$ into three Stark components. Since the excitation line is well matched with overlapping CT transitions both Eu^{3+} sites are excited mutually and all Stark components of the two different emitting centers should be observed. Accordingly with the spectra in Fig. 10 and 11 more components are visible ${}^5\text{D}_0 \rightarrow {}^7\text{F}_1$ than expected from the theoretical data. It most probably means that due to the charge compensation effects the symmetry of the C_3 site is lowered and/or there is a presence of some Eu^{3+} ions, with low symmetry, located at nanoparticle surface or close-to-surface area quite common in nanoparticles. The latter explanation might also be supported by visible shoulders for the ${}^5\text{D}_0 \rightarrow {}^7\text{F}_0$ transition connected with surface optical centers.

It is well known that the electric dipole ${}^5\text{D}_0 \rightarrow {}^7\text{F}_2$ transition is highly prone to even slight changes of the local surrounding whereas the ${}^5\text{D}_0 \rightarrow {}^7\text{F}_1$ magnetic dipole transition

should remain practically independent on the host lattice. Therefore, the magnetic dipole transition is usually treated as an internal reference. In general, when Eu^{3+} ions substitutes position with the centre of symmetry the only one allowed transition is the magnetic one $^5\text{D}_0 \rightarrow ^7\text{F}_1$. In the opposite case the electric dipole $^5\text{D}_0 \rightarrow ^7\text{F}_2$ becomes dominant³³ being exactly the case in our studies. Furthermore, it has been proposed that the ratio between the integral intensities of the both transitions $^5\text{D}_0 \rightarrow ^7\text{F}_2$ and $^5\text{D}_0 \rightarrow ^7\text{F}_1$ could be used for evaluation of the Eu^{3+} polyhedron coordination asymmetry R defined as follows:

$$R = \frac{\int ^5D_0 \rightarrow ^7F_2}{\int ^5D_0 \rightarrow ^7F_1} \cdot (3)$$

The consequence of that is as follows the higher the I_{0-2}/I_{0-1} ratio is, the more apart from a centrosymmetric geometry Eu^{3+} is³⁴. In fact the asymmetry parameter R changes progressively with Eu^{3+} concentration increase from 8 to almost 12 (Table 3). Hence, the conclusion might be drawn that the local environment of the Eu^{3+} becomes more distorted upon doping. This would be also logical since incorporation of more +3 ions into +2 site would actually induce more network defects.

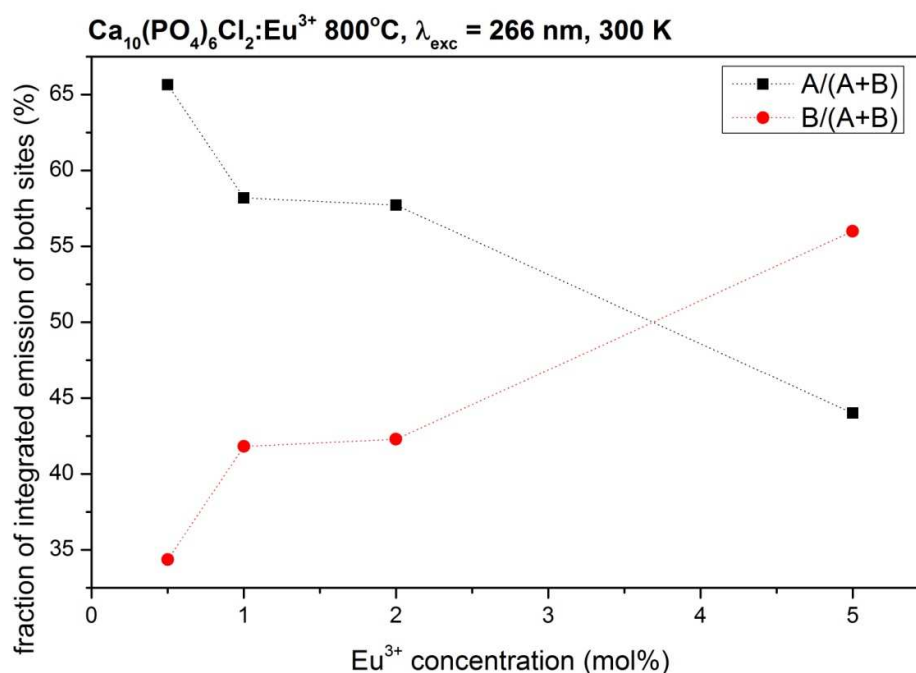


Figure 12. Eu^{3+} site occupancy changes represented as a fraction of the $^5\text{D}_0 \rightarrow ^7\text{F}_0$ integral intensities vs Eu^{3+} concentration.

It is worth noting the dependence of the Eu^{3+} ions concentration on the sites occupation preference shown in Figure 12. The problem of the site preference of several rare earth

elements in calcium chloroapatite structure have been discussed by Fleet *et al.* **Error! Bookmark not defined.** using crystallographic approach but not exploiting indirect optical techniques. In our earlier article devoted to the calcium hydroxyapatite the site preference studies were conducted using analysis of the Eu^{3+} ions luminescence behavior⁶. In comparison with both approaches it could be concluded that indeed for low concentration range of RE^{3+} ions would preferentially substitute the *A* site whereas increase of dopant amount would lead to reverse dependence. As it can be seen up to 0.5 mol% of the Eu^{3+} the ${}^5\text{D}_0 \rightarrow {}^7\text{F}_0$ ascribed to the *A* site dominates and further increase of the Eu^{3+} concentration above 2 mol% results in domination of the Eu^{3+} cations at *B* site (see Figure 9 and compare with emission spectra). At last accordingly with structural data domination of *B* site is not a surprise upon exceeding critical Eu^{3+} concentration since the ratio between *A* and *B* site is 2:3 (*A* – 4f, *B* – 6h). Therefore utilization of the Eu^{3+} ions as an optical probe is a straightforward method for solving structural features of the given host lattice and does not need sophisticated calculation methods to be used. Moreover, it was also interesting to test not only the concentration effect but also how the sintering temperature would influence the site preference of the Eu^{3+} cations in the $\text{Ca}_{10}(\text{PO}_4)_6\text{Cl}_2$ matrix (Figure 13 and 14). A brief comparison draws a conclusion that the higher annealing temperature the more Eu^{3+} ions are incorporated at *A* crystallographic site.

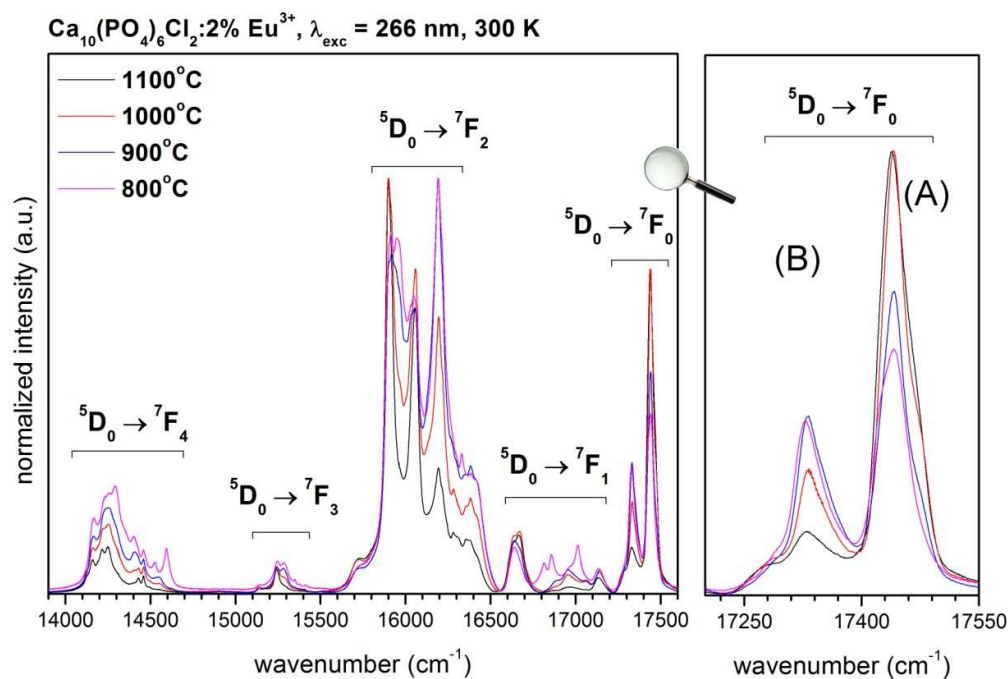


Figure 13. Emission spectrum of the $\text{Ca}_{10}(\text{PO}_4)_6\text{Cl}_2: 2\% \text{Eu}^{3+}$ as function sintering temperature measured at 300 K, $\lambda_{\text{exc}} = 266 \text{ nm}$.

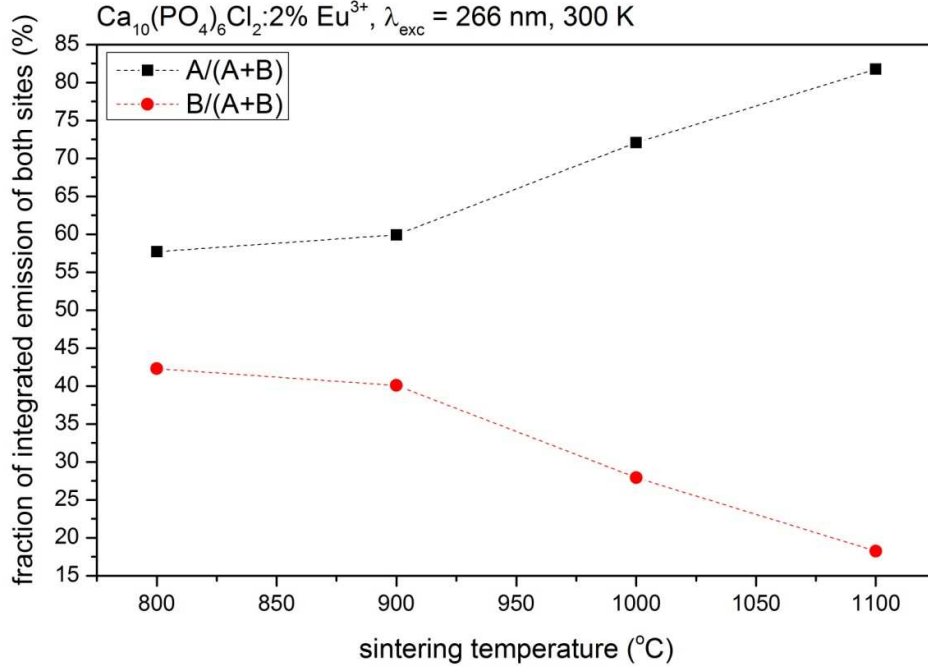


Figure 14. Eu^{3+} site occupancy changes represented as a fraction of the ${}^5\text{D}_0 \rightarrow {}^7\text{F}_0$ integral intensities vs sintering temperature.

In order to get a deeper insight into the nature of the luminescence behaviour of the Eu^{3+} in the $\text{Ca}_{10}(\text{PO}_4)_6\text{Cl}_2$, the intensity parameters Ω_2 and Ω_4 can be determined using approach described previously by Kodaira³⁵, Werts³⁶ and Hreniak³⁷. Relation between the ${}^5\text{D}_0 \rightarrow {}^7\text{F}_J$ transitions was used to determine the Ω_λ parameters assuming that the matrix element $U^{(6)}$ is close to zero for the ${}^5\text{D}_0 \rightarrow {}^7\text{F}_6$ transition ($U^{(6)} = 0.0005$). Therefore matrix elements for transitions from the ${}^5\text{D}_J$ ($J = 0, 1, 2$, and 3) are zero³⁸. The Einstein coefficients $A_{0-\lambda}$ for spontaneous emission is defined as follows:

$$A_{0-\lambda} = \frac{64\pi^4\nu^3e^2}{3hc^3} \frac{1}{4\pi\epsilon_0} \chi \sum_{\lambda=2,4} \Omega_\lambda \langle {}^5\text{D}_0 \| U^{(\lambda)} \| {}^7\text{F}_J \rangle^2. \quad (4)$$

Due to the “clearing” matrix elements $U^{(4)}$, $U^{(6)}$ and $U^{(2)}$, $U^{(6)}$ for the ${}^5\text{D}_0 \rightarrow {}^7\text{F}_2$ and ${}^5\text{D}_0 \rightarrow {}^7\text{F}_4$ transitions, respectively, the values of the Ω_2 and Ω_4 can be extracted by determining $A_{0-\lambda}$ directly from emission spectra taking $\langle {}^5\text{D}_0 \| U^{(2)} \| {}^7\text{F}_2 \rangle = 0.0035$ and $\langle {}^5\text{D}_0 \| U^{(4)} \| {}^7\text{F}_4 \rangle = 0.0030$, respectively. This can be done by taking the relation between the integral intensity I and the transition energy $h\nu$ given as $I = h\nu AN$, where A is the Einstein coefficient for spontaneous emission and N is the population of the emitting ${}^5\text{D}_0$ level. By the comparison of both sides of the equations describing the ${}^5\text{D}_0 \rightarrow {}^7\text{F}_2$ and ${}^5\text{D}_0 \rightarrow {}^7\text{F}_4$ transitions to N , the expression for $A_{0-\lambda}$ has now following form:

$$A_{0-\lambda} = A_{0-J} = A_{0-1} \frac{I_{0-J}}{I_{0-1}} \frac{h\nu_{0-1}}{h\nu_{0-J}}, \quad (5)$$

where I_{0-J} , $h\nu_{0-J}$ and I_{0-1} , $h\nu_{0-1}$ are the integral intensities and energies of the ${}^5D_0 \rightarrow {}^7F_1$ and ${}^5D_0 \rightarrow {}^7F_1$ transitions, respectively. In simplified Judd-Ofelt theory (J-O) the A_{0-1} coefficient corresponding to the ${}^5D_0 \rightarrow {}^7F_1$ transition has to be fixed at some reasonable value. Therefore 36.5 s^{-1} was assumed due to the magnetic character of the ${}^5D_0 \rightarrow {}^7F_1$ transition and its weak dependence on the crystal field effects^{6,28}. Following the magnitudes of decay rates ($A_{J-J'}$) determined from the excited 5D_0 level it is now possible to estimate the radiative decay rate (A_{rad}):

$$A_{\text{rad}} = \sum_J A_{J-J'} \quad (6)$$

Additionally, by taking the measured luminescence lifetimes the non-radiative (A_{nrad}) and total decay rate (A_{tot}) are expressed as:

$$A_{\text{tot}} = \frac{1}{\tau} = A_{\text{rad}} + A_{\text{nrad}} \quad (7)$$

Eventually having radiative and non-radiative decay rates the quantum efficiency of overall luminescence can be easily calculated:

$$\eta = \frac{A_{\text{rad}}}{A_{\text{rad}} + A_{\text{nrad}}} \quad (8)$$

All the results of calculation using simplified J-O theory have been gathered in table 3.

Table 3. Decay rates of radiative (A_{rad}), non-radiative (A_{nrad}) and total (A_{tot}) processes of ${}^5D_0 \rightarrow {}^7F_1$ transitions, luminescence lifetimes (τ), intensity parameters (Ω_2 , Ω_4), quantum efficiency (η) and asymmetry ratio (R) determined from photoluminescence spectra of the $\text{Ca}_{10}(\text{PO}_4)_6\text{Cl}_2:\text{Eu}^{3+}$ treated at 800°C .

| Sample | $A_{\text{rad}} (\text{s}^{-1})$ | $A_{\text{nrad}} (\text{s}^{-1})$ | $A_{\text{tot}} (\text{s}^{-1})$ | τ (ms) | $\Omega_2 (10^{-20} \text{ cm}^2)$ | $\Omega_4 (10^{-20} \text{ cm}^2)$ | η (%) | R |
|------------|----------------------------------|-----------------------------------|----------------------------------|-------------|------------------------------------|------------------------------------|------------|-------|
| 0.5 | 421.65 | 219.37 | 641.02 | 1.56 | 0.113 | 6.134 | 65.78 | 8.14 |
| 1 | 405.01 | 231.93 | 636.94 | 1.57 | 0.106 | 6.198 | 63.58 | 7.67 |
| 2 | 502.94 | 389.91 | 892.85 | 1.12 | 0.138 | 7.144 | 56.33 | 9.96 |
| 5 | 585.12 | 255.22 | 840.34 | 1.19 | 0.164 | 7.954 | 69.63 | 11.87 |

It is worth noting that the magnitude of Ω_2 and Ω_4 parameters increase with the Eu^{3+} ions concentration. The mutual change of asymmetry parameter R follows the same trends as Ω_2 pointing out on the increased distortion of the Eu^{3+} cations polyhedra as well as could be related to the slight change in the $\text{Eu}^{3+}-\text{O}^{2-}$ bond covalence increasing with doping. On the other hand the value of the Ω_4 cannot be directly associated with the symmetry changes of the Eu^{3+} ions but could give some information about changes of the electron density on the

surrounding O^{2-} anions³⁹. The quantum efficiency (η) was estimated theoretically from J-O calculations giving rather close to each other values being around 65 %. There is a small irregularity for quantum efficiency with the increase of dopant concentration that is connected with a fraction of atoms located on the nanomaterial surface or close-to-surface regions that are more prone to the quenching due to the easier contact with impurities (such as H_2O , $-OH$ groups and etc.). Therefore increase of the Eu^{3+} ions concentration with keeping the size of the particle would increase the number of optical centres in such regions contributing to decrease of QE due to the increase of non-radiative processes.

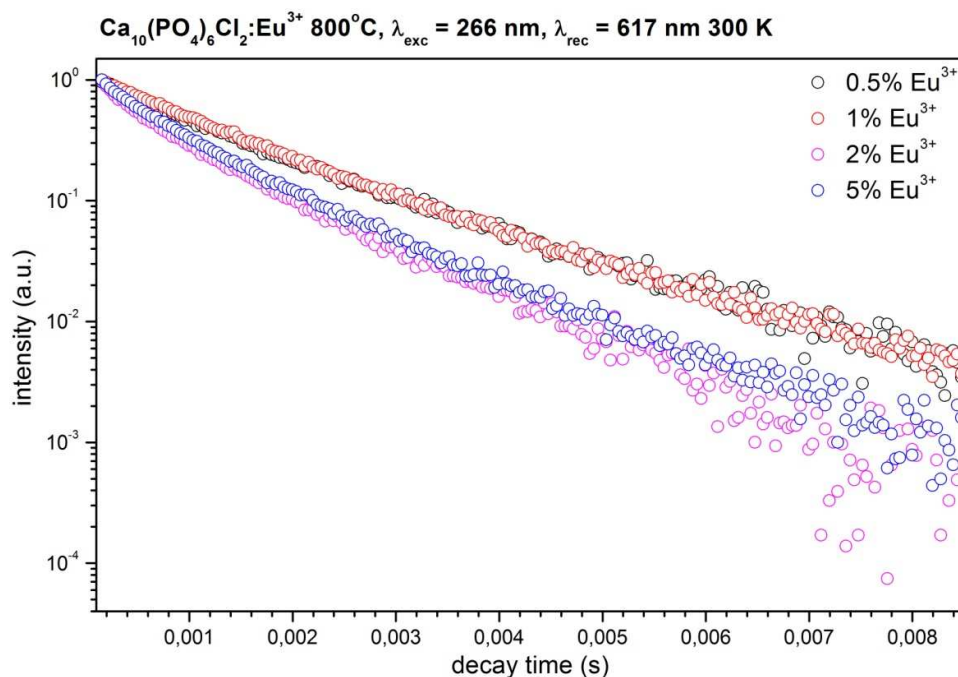


Figure 15. Decay profiles of the $Ca_{10}(PO_4)_6Cl_2:Eu^{3+}$ as a function of the dopant concentration.

The luminescence kinetics studies of the $Ca_{10}(PO_4)_6Cl_2:Eu^{3+}$ as a function of dopant concentration related to the ${}^5D_0 \rightarrow {}^7F_2$ emission were performed at room temperature (see Figure 15) upon excitation at 266 nm. As it can be seen the decay profiles are not single exponential for all studied cases. Since the physical sense of the fitting with multi-exponential dependence is difficult to interpret the values of lifetimes were calculated as the effective emission decay time using following expression:

$$\tau_m = \frac{\int_0^{\infty} tI(t)dt}{\int_0^{\infty} I(t)dt} \cong \frac{\int_0^{t^{max}} tI(t)dt}{\int_0^{t^{max}} I(t)dt}, \quad (9)$$

where $I(t)$ represents the luminescence intensity at time t corrected for the background and the integrals are evaluated on a range $0 < t < t^{max}$ where $t^{max} \gg \tau_m^{40}$. It was found that the effective decay time decreases (from 1.57 to 1.19 ms) significantly with increase of amount of the Eu^{3+} ions (see Table 3). Thus, this behavior can be attributed to the concentration quenching phenomena relying on the energy transfer between the interacting activator ions⁴¹. For the effective energy transfer distance between activators has to be below certain value called critical distance R_c which can be calculated by:

$$R_c \approx 2 \left(\frac{3V}{4\pi\chi_c N} \right)^{1/3}, \quad (10)$$

where V is the volume of the unit cell, N is the number of cations which can be substituted by the dopant per unit cell and χ_c is the critical concentration of the dopant at which the concentration quenching occurs. In the case of the $\text{Ca}_{10}(\text{PO}_4)_6\text{Cl}_2:\text{Eu}^{3+}$ the V is 537.64 \AA^3 , Z equals 10 and χ_c is 0.02 (2%), respectively. The critical transfer distance of the Eu^{3+} in $\text{Ca}_{10}(\text{PO}_4)_6\text{Cl}_2$ is calculated to be about 17 \AA . For the resonant energy transfer two mechanism are involved exchange and multipolar interactions. The former one is valid when critical distance is less than 4 \AA thus in this particular case energy transfer in the $\text{Ca}_{10}(\text{PO}_4)_6\text{Cl}_2$ will be caused by the multipole interactions only. Thus emission intensity (I) per activator follows the equation:

$$\frac{I}{\chi} = K[1 + \beta(\chi)^{Q/3}]^{-1}, \quad (11)$$

where I is the emission intensity per activator ion, χ is the activator concentration, K and β are constants under the same excitation condition for the given host crystal and Q is a constant of multipolar interaction and equals 6, 8 or 10 for dipole-dipole, dipole-quadrupole or quadrupole-quadrupole interaction, respectively. If $\beta\chi^{Q/3} \gg 1$, then Eq. 5 is reduced to:

$$\lg\left(\frac{1}{\chi}\right) = A - \frac{Q}{3} \lg \chi, \quad (12)$$

where $A = \lg K - \lg \beta$ ⁴². Out of this relation slope value of -1.28 was extracted meaning that the Q value is close to 6. Hence the major mechanism responsible for concentration quenching will be a dipole-dipole one.

4. Conclusions

The Eu^{3+} doped $\text{Ca}_{10}(\text{PO}_4)_6\text{Cl}_2$ nanocrystalline powders were successfully synthesized using microwave stimulated technique. Additional post heat treatment at the range of temperature $800 - 1100 \text{ }^\circ\text{C}$ was applied in order to improve crystallinity of the final product

and eliminate residual amorphous phase. The concentration range of optically active ions was set to be 0.5 – 5 mol% to investigate the solubility levels and site occupancy preference. The calculated size of particles is strongly dependent on sintering temperature being 80 nm for the $\text{Ca}_{10}(\text{PO}_4)_6\text{Cl}_2$ treated at 800°C and increases progressively with temperature up to 180 nm. TEM images confirmed nano nature of the final product giving the value of the primary size around 60 nm in dry powders and value of the hydrodynamic size of 200 nm when dispersed in MQ-water without further stabilization. In fact, on one hand influence of the dopant concentration relies on observed formation of traces of the secondary EuPO_4 phase once amount of the Eu^{3+} exceeds 2 mol% achieving the critical solubility. On the other basing on the luminescence properties of the Eu^{3+} it has been found that for low concentration *A* site is preferentially substituted whereas increase of Eu^{3+} above 2 mol% results in domination of the Eu^{3+} cations located at *B* site. Consecutive red shift of the CT band with dopant concentration increase was observed strongly evidencing on incorporation of the Eu^{3+} ions at *B* site. The analysis of behavior of the both ${}^5\text{D}_0 \rightarrow {}^7\text{F}_0$ transitions points out on the domination of the Eu^{3+} positioned at *A* site for low concentrated samples and *B* site at high amounts of the Eu^{3+} . It was also interesting to note that increase of sintering temperature leads to increase of intensity of the ${}^5\text{D}_0 \rightarrow {}^7\text{F}_0$ line associated with the Eu^{3+} at *A* site. Therefore conclusion might be drawn that the site preference problem in many types of materials might be solved using relatively simple analysis of luminescent properties of the Eu^{3+} cation. Basing on the simplified J-O theory it was found that the magnitude of Ω_2 and Ω_4 parameters increase with the Eu^{3+} ions concentration. The mutual change of asymmetry parameter *R* and Ω_2 points out on the increased distortion of the Eu^{3+} polyhedra as well as could be related to the change in the $\text{Eu}^{3+}\text{-O}^{2-}$ bond covalence increasing upon doping. The dependence of the Ω_4 cannot be directly associated with the symmetry changes of the Eu^{3+} ions but could give some information about changes of the electron density on the surrounding O^{2-} anions influencing the position of the CT band eventually. The mechanism of concentration quenching process was identified as a dipole-dipole interaction occurring within pairs of the Eu^{3+} ions above certain critical concentration.

Acknowledgements

The authors would like to thank M.Sc. Ewa Bukowska for performing XRD measurements, Ph.D. Malgorzata Malecka for the access to TEM instrumentation as well M.Sc. Karolina Mokrzycka for help with sample synthesis. Financial support of the National Science Centre

in course of realization of the Project ‘Nanomaterials for fluorescence lifetimes bio-imaging (NFLBio)’ (no. UMO-2012/06/M/ST5/00048) is gratefully acknowledged.

References

- ¹ S. Santra, P. Zhang, K. Wang, R. Tapeç, W. Tan, *Anal. Chem.*, **2001**, 73, 4988.
- ² H. Zhang, X.J. Ye, J.S. Li, *Biomed Mater.*, **2009**, 4, 45007.
- ³ A. Doat, F. Pelle, N. Gardant, A. Lebugle, *J. Solid State Chem.*, **2004**, 1777, 1179.
- ⁴ P. Martin, G. Carlot, A. Chevarier, C. Den-Auwer, G. Panczer, *J. Nucl. Mater.*, **1999**, 275, 268–276.
- ⁵ R. Sahoo, S.K. Bhattachary, and R. Debnath, *J. Solid State Chem.*, **2003**, 175, 218-225 and references therein.
- ⁶ R.J. Wıglusz, A. Bednarkiewicz, A. Łukowiak, W. Stręk, *Spectr. Lett.*, **2010**, 43, 1.
- ⁷ R.J. Wıglusz, A. Kedziora, A. Lukowiak, W. Doroszkiewicz, W. Strek, *J. Biomedical Nanotech.*, **2012**, 8, 1.
- ⁸ P.H. Schlesinger, H.C. Blair, S.L. Teitalbaum, J.C. Edwards, *J. Biol. Chem.*, **1997**, 272, 18636.
- ⁹ S. Kannan, A. Rebelo, J.M.F. Ferreira, *J. Inorg. Biochem.*, **2006**, 100, 1692.
- ¹⁰ M. Fleet, X. Liu, Y. Pan, *Am. Miner.*, **2000**, 85, 1437.
- ¹¹ G. K. Lim, J. Wang, S. C. Ng, L. M. Gan, *J. Mater. Chem.*, **1999**, 9, 1635.
- ¹² E. Jallot, H. Benhayoune, L. Kilian, J.L. Irigaray, G. Balossier, P. Bonhomme, *J. Phys. D: Appl. Phys.*, **2000**, 33, 2775.
- ¹³ J. Andersson, S. Areva, B. Spliethoff, M. Lindén, *Biomater.*, **2005**, 26, 6827.
- ¹⁴ Card No. 24237 ICDS, Fachinformationszentrum Karlsruhe, 2012.
- ¹⁵ Card No. 79752 ICDS, Fachinformationszentrum Karlsruhe, 2012.
- ¹⁶ R.D. Shannon, *Acta Cryst.*, **A32**, 751 (1976).
- ¹⁷ H.M. Rietveld: *J. Appl. Cryst.* **2** (1969), 65.
- ¹⁸ R. Delhez, T.H. de Keijser, J.I. Langford, D. Louër, E.J. Mittemeijer and E.J. Sonneveld, Crystal Imperfection Broadening and Peak Shape in the Rietveld Method, in: *The Rietveld Method*, edited by R.A. Young, Oxford Science, Oxford, United Kingdom (1993), 132.
- ¹⁹ L. Lutterotti and P. Scardi, *J. Appl. Cryst.*, **1990**, 23, 246.
- ²⁰ L. Lutterotti, S. Matthies and H.-R. Wenk, *IUCr: Newsletter of the CPD*, **1999**, 21, 14.
- ²¹ H. El Feki, M. Amami, A. Ben Salah, M. Jemal, *Phys. Stat. Sol. C*, **2004**, 1, 1985-1988.
- ²² G. Montel, G. Bonel, J. C. Heughebaert, J. C Trombe, C. Rey, *J. Cryst. Growth*, **1981**, 53, 74.
- ²³ J. Goldstein, D. Newbury, D. Joy, C. Lyman, P. Echlin, E. Lifshin, L. Sawyer, J. Michel, *Scanning electron microscopy and X-ray microanalysis*, Springer, New York, 2007.
- ²⁴ K.W. Powers, S.C. Brown, V.B. Krishna, S.C. Wasdo, B.M. Moudgil, S.M. Robert, *Toxic. Sci.*, **2006**, 90, 296.

-
- ²⁵ R.Pazik, E. Piasecka, M. Małecka, V.G. Kessler, B. Idzikowski, Z. Śniadeckie, R.J. Wiglusz, RSC Advances, **2013**, 3, 12230.
- ²⁶ R.J. Wiglusz, A. Watras, M. Malecka, P.J. Deren and R. Pazik, Eur. J. Inorg. Chem., DOI: 10.1002/ejic.201301351
- ²⁷ Blasse G., Structure and Bonding, Berlin, **1976**, 26, 43.
- ²⁸ R.J. Wiglusz, R. Pazik, A. Łukowiak, W. Stręk, *Inorg. Chem.*, **2011**, 50, 1321.
- ²⁹ R.J. Wiglusz, T. Grzyb, A. Bednarkiewicz, S. Lis, W. Strek, *Eur. J. Inorg. Chem.*, **2012**, 21, 3418.
- ³⁰ D. Hreniak, W. Strek, J. Amami, Y. Guyot, G. Boulon, C. Goutadier, R. Pazik, *J. Alloys Compd.*, **2004**, 380, 348.
- ³¹ R. Pazik, A. Watras, L. Macalik, P.J. Deren, *New J. Chem.*, DOI: 10.1039/C3NJ01168B.
- ³² X. Wei, G.C. Jiang, Y.G. Qin, Y.H. Chen, C.K. Duan, M. Yin, *J. Lumin*, **2014**, 146, 371-375.
- ³³ J.C.G. Bünzli, G.R. Choppin, Lanthanide Probes in Life Chemical and Earth Sciences. Theory and Practice, Elsevier, Amsterdam, **1979**, Chapter 35.
- ³⁴ E.W.J.L. Oomen, A.M.A. van Dongen, *J. Non-Cryst. Solids*, **1989**, 111, 205.
- ³⁵ C.A. Kodaira, H.F. Brito, O.L. Malta, O.A. Serra, *J. Lumin.*, **2003**, 101, 11.
- ³⁶ M.H.V. Werts, R.T.F. Jukers, J.W. Verhoeven, *Phys. Chem. Chem. Phys.*, **2002**, 4, 1542.
- ³⁷ D. Hreniak, W. Strek, J. Amami, Y. Guyot, G. Boulon, C. Goutaudier, R. Pazik, *J. Alloys. Comp.*, **2004**, 380, 348.
- ³⁸ H.S. Kiliaan, J.F.A.K. Kotte, G. Blasse, *Chem. Phys. Lett.*, **1987**, 133, 425.
- ³⁹ Y. Nageno, H. Takebe, K. Morinaga, *J. Am. Ceram. Soc.*, **1993**, 76, 3081.
- ⁴⁰ R. Pazik, D. Hreniak, W. Strek, A. Speghinin, M. Bettinelli, *Opt. Mater.*, **2006**, 28, 1284-1288.
- ⁴¹ G. Blasse, *Philips Res. Rep.*, **1969**, 24, 131-144.
- ⁴² L.G.V. Uitert, *J. Electrochem. Soc.*, **1967**, 114, () 1048-1053.